

Thin liquid films in a funnel

T.-S. Lin¹, and J.A. Dijkstra², and L. Kondic³

¹Department of Applied Mathematics, National Yang Ming Chiao Tung University, Hsinchu 30010, Taiwan

²Physical Chemistry and Soft Matter, Wageningen University & Research, Stippeneng 4, 6708WE Wageningen, The Netherlands

³Department of Mathematical Sciences and Center for Applied Mathematics and Statistics, New Jersey Institute of Technology, Newark, New Jersey 07102, USA

(Received ?; revised ?; accepted ?. - To be entered by editorial office)

We explore flow of a completely wetting fluid in a funnel, with particular focus on contact line instabilities at the fluid front. While the flow in a funnel may be related to a number of other flow configurations as limiting cases, understanding its stability is complicated due to the presence of additional azimuthal curvature, as well as due to convergent flow effects imposed by the geometry. Convergent nature of the flow leads to thickening of the film, therefore influencing its stability properties. In this work, we analyze these stability properties by combining physical experiments, asymptotic modeling, self-similar type of analysis and numerical simulations. We show that appropriate long-wave based model supported by the input from experiments, simulations and linear stability analysis origination from the flow down an incline plane provides a basic insight allowing to understand the development of contact line instability and emerging lengthscales.

1. Introduction

Thin liquid films with fronts involving contact lines and their instabilities are relevant to applications in a number of different fields, ranging from nanoscale to macroscale films where instabilities are driven by a combination of various body forces, surface tension, and wettability, see [Oron *et al.* \(1997\)](#); [Craster & Matar \(2009\)](#) for reviews. Significant progress has been reached by using long wave approximation, which simplifies considerably the analysis of thin film flows and their stability. In the context of thin films on a macroscale, the setup involving completely wetting film of constant thickness flowing down an incline has been understood reasonably well. For such configuration, linear stability analysis (LSA) carried out in a moving reference frame leads to the dispersion relation which shows stability for large wavenumbers, and predicts the most unstable wavelength (specifying the distance between emerging fingers), which results from the balance between destabilizing gravity and stabilizing surface tension forces, see e.g. [Troian *et al.* \(1989\)](#); [Bertozi & Brenner \(1997\)](#). However, as soon as some of the simplifying assumptions are removed, understanding the instability becomes much more complicated.

In the present paper, we focus on the funnel geometry, see figure 1, where initially a fixed amount of wetting fluid is deposited around a perimeter and then let to evolve due to gravity. Despite its relevance to a number of practical applications, funnel flow to the best of our knowledge has not been yet carefully analyzed, in particular in the context of front instabilities. Funnel flow involves geometry-induced convergence, and the influence of this convergence, as well as of azimuthal curvature on instability development is unknown. For the purpose of understanding stability properties of a film in a funnel, it is useful to discuss some of the many limiting configurations that could be related to the considered one.

If the film is deposited at a sufficient distance from the centre, the azimuthal curvature is small, and one could relate the problem to the finite volume of fluid deposited on an incline plane. Even that problem is, however, difficult to analyze due to a time-dependent base state, see [Goodwin & Homsy \(1991\)](#); [Gomba *et al.* \(2007\)](#). The limiting case of the opening angle $\alpha = 90^\circ$ could be thought of as a flow down a cylinder (in a direction of the cylinder axis) ([Smolka & SeGall 2011](#); [Mayo *et al.* 2013](#)), which shows fingering type of instabilities. Fingering instability is also observed for the flow down a surface of a cylinder or a sphere ([Takagi & Huppert 2010](#); [Balestra *et al.* 2019](#)), the setup which shows similarity to fingering observed during spin coating ([Melo *et al.* 1989](#); [Frayssse & Homsy 1994](#)). Another setup of interest is flow in a Hele-Shaw geometry where surface geometry plays a role in instability development, see [Miranda *et al.* \(2000\)](#); [Brandão *et al.* \(2014\)](#). In the limit $\alpha = 0^\circ$, one could think of the problem of closing a hole in a film on a horizontal substrate ([Diez *et al.* 1992](#)), which is stable ([Backholm *et al.* 2014](#); [Bostwick *et al.* 2017](#); [Zheng *et al.* 2018](#); [Lv *et al.* 2018](#)). Another possibly relevant limit is that of a liquid filament, which on a horizontal substrate becomes unstable by a mechanism that could be related to Rayleigh-Plateau instability of a liquid jet, modified by the presence of a substrate ([Davis 1980](#)). That problem is, however, difficult to analyze in the limit of zero contact angle that we consider here, see [Diez *et al.* \(2009\)](#). Perhaps closer analogy is fluid ring on a horizontal substrate, which indeed may become unstable ([Gonzalez *et al.* 2013](#)). However, the fact that there is no body force inducing converging flow makes this setup significantly different from the funnel flow. Converging nature of the flow in a funnel leads to thickening of the film, and since the film thickness is important in determining both the speed of spreading, and the instability mechanism itself, it is expected to influence the instability considerably. We should also point out that the problem opposite to our setting, rising film in a glass, was considered recently ([Dukler *et al.* 2020](#)).

Various limiting cases suggest many possible routes for analysis of the instability evolution. In the present paper, we start by discussing our experimental results in [Sec. 2](#), and then follow in [Sec. 3](#) by considering appropriate models for describing spreading of a film on curved substrates. In [Sec. 4](#) we discuss first generic features of the funnel flow, by discussing similarities and differences to the flow down an incline, with particular focus on the regime such that useful input can be obtained by applying a self-similar approach. Then, in [Sec. 4.2](#) we apply the insights obtained in [Sec. 4.1](#) to interpret the experimental results, with particular focus on the instability development. [Section 5](#) concludes the main part of the paper. The LSA for a liquid film of constant flux flowing down an incline is briefly discussed in the Appendix. Supplementary materials ([Lin *et al.* 2020](#)) provide some technical details, experimental videos as well as the complete list of experimental results.

2. The experiment

We designed funnels with Solidworks and 3D printed them on a fused-deposition 3D printer. [Figure 1](#) shows the details of the funnels. Inside the funnel, we glue a thin latex sheet, which helps create a smoother surface. The funnel is placed between a green light source and a beaker that collects the liquid flowing out of the funnel opening. To prepare the experiment, a 3D printed stopper of radius $S = 6$ cm is inserted in the funnel, see [figure 1\(b\)](#). A known volume of fluid, V , is then carefully deposited around the funnel using a syringe; the fluid spreads itself evenly in the cavity around the stopper. This creates an initial film of height h_i (measured in the vertical direction), which we use as our control parameter to simplify interpretation of the results (note that $V \approx \pi S h_i^2 / \tan \alpha$). For every trial, the funnel and stopper are cleaned and leveled before deposition. For small

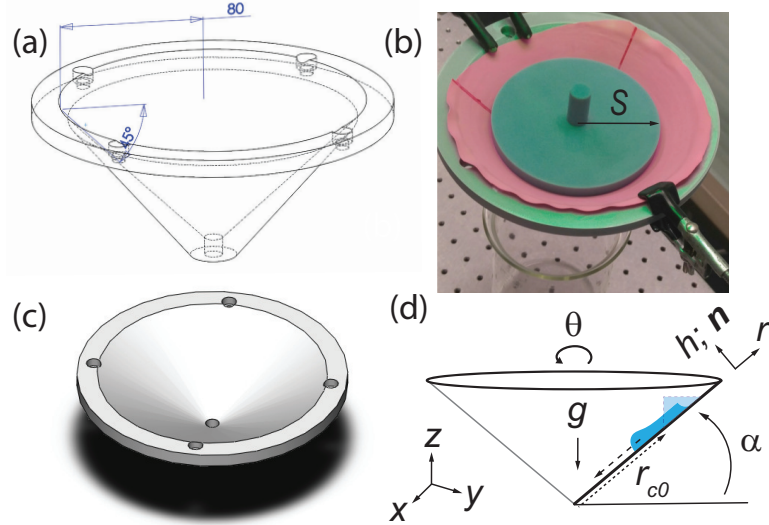


FIGURE 1. (Color online) (a) Solidworks wire sketch of the 47° funnel. Note that the technical drawing mentions 45° ; printing imperfections can somewhat modify the opening angle, which is therefore always measured after printing. (b) Photo of the experimental setup including the latex sheet, stopper and green light illumination. The beaker that collects the PDMS is visible underneath the funnel. S indicates the radius of the stopper used as initial barrier that releases the fluid. (c) Solidworks drawing of the 35° funnel. (d) Coordinate system variables used in the description of the fluid behavior (solid lines). The light blue surface delineated with the dotted line indicates the initial fluid volume and position as created by the stopper at distance r_{c0} (dotted arrow) from the origin of the funnel geometry; the thickness of the film referenced in the text, h_i , is measured in the vertical direction (therefore, along the short stopper dimension). The dashed arrow indicates the flow direction of the thin film. The arrow denoted by g indicates the direction of gravity.

values of the opening angle, α , one needs a prohibitively large V to keep h_i in a range that is also appropriate for larger α , so for such angles we choose smaller values of h_i . To start the flow, the stopper is raised and flow is observed. A fluorescent dye (Pyrromethene) is added to the fluid stock solution, enhancing the contrast between the moving fluid and the latex sheet under influence of the green light. We use polydimethylsiloxane (PDMS) of density $\rho = 9.6 \times 10^2 \text{ kg/m}^3$, viscosity $\mu = 1 \times 10^3 \text{ mPa}\cdot\text{s}$, and surface tension $\gamma = 21 \text{ mN m}^{-1}$; for more details regarding PDMS properties see [Dijksman *et al.* \(2019\)](#). Note that PDMS wets latex, since the critical surface-vapor surface tension of typical latex types $\approx 50 \text{ mJ/m}^2$ is much higher than the low surface tension of PDMS $\approx 20 \text{ mJ/m}^2$; see [Ho & Khew \(2000\)](#) and [Zhang *et al.* \(2018\)](#). This means that the spreading parameter is larger than 0 and that thus the contact angle is zero, without hysteresis (see e.g. the book from [De Gennes *et al.* \(2004\)](#)). Elastocapillary effects such as discussed in [Marchand *et al.* \(2012\)](#) are neglected as the ratio of liquid-vapor surface tension to elastic modulus of the latex rubber is much smaller than the thickness of the latex sheet $\approx 1 \text{ mm}$. Fluid flow is recorded using a high resolution camera at 25 frames per second. The videos serve both to extract the wavelength of the developing instability and for the quantitative assessment of the flow speeds of the relevant film features.

It should be pointed out that there are few experimental issues that lead to some variation in the extracted experimental results discussed later in the text (and denoted by error bars where appropriate). At first, the method to distribute the fluid, while simple, may not have always led to a perfect azimuthally symmetric distribution. Another

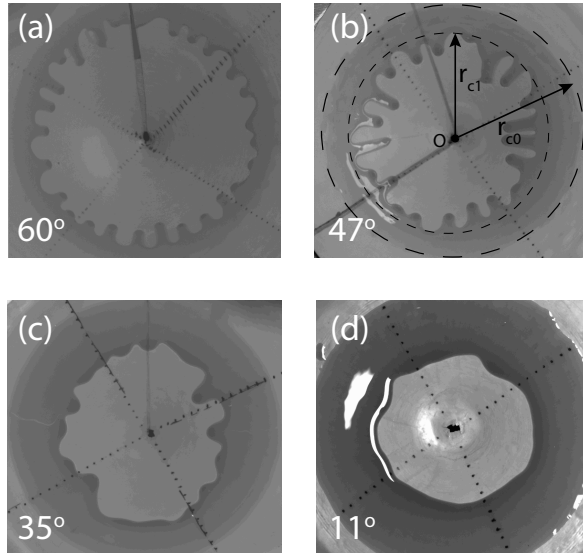


FIGURE 2. (a-d) Flow examples for the 60, 47, 35 and 11 degree opening angles, respectively. The width of each image is ≈ 60 mm, as indicated by the dark circle that demarcates the edge of the fluid volume before onset of the flow. See also (a) *Video1*; (b) *Video2*; (c) *Video3*; (d) *Video4*.

source of error is the formation of air pockets under the thin rubber sheet lining the funnels. Re-gluing prior to conducting experiments helped to create a surface free of larger surface abnormalities. Conducting multiple experiments and averaging the values helped to remedy some of these errors and reduce the error bars. More detailed information regarding the experiments, including selected experimental videos (*Videos 1 - 4*) as well as funnel specifications (*Drawing1*, *Drawing2*) are available (Lin *et al.* 2020); additional videos can be found at the NJIT Capstone Laboratory web page (Kondic 2019).

2.1. Extracting instability features

The videos allow us to extract two main features of the instability: the number of fingers observed, N_{exp} , and the onset radius of fingering, r_{c1} . We show snapshots from top view videos for four values of α to identify such features in figure 2(a-d). The experiments for each set of parameters are repeated several times to obtain conclusive results, which are summarized in Table 1 that shows N_{exp} , as observed for a few different values of α and h_i . We have also carried out additional experiments using PDMS of lower viscosity, $\mu = 3.5 \times 10^2$ mPa s, which show that N_{exp} is viscosity-independent, the point to which we return in Sec. 4.2. Before closing this section, we note that the rear contact line remains essentially fixed, with the fluid thinning in its vicinity, as it can be seen clearly in the supplementary videos (Lin *et al.* 2020). This point will become relevant later when considering the self-similar solution.

2.2. Extracting front speed

To extract flow speed we need to extract quantitative data from the videos. In particular, we extract the finger tip position as a function of time. First, we need to know where r_{c1} is, the onset position of fingering. Figure 3(a) illustrates in more detail our approach to finding this value. We define r_{c1} by requiring that at the onset of fingering, the distinct

α (degrees)	V (ml)	r_{c0} (mm)	r_{c1} (mm)	h_i (mm)	N_{exp} (-)
60	2.8	120	110 ± 0.7	5	27 ± 1.2
	5.4	120	112	7	23
47	4.5	88	77 ± 1.2	5	21 ± 0.8
	8.9	88	75 ± 2.3	7	16 ± 0.5
35	6.9	73	57	5	16
11	6.7	61	47 ± 3	2.5	10 ± 2.8
	9.7	61	50	3	10
	17.8	61	43	4	6

TABLE 1. Experimental results for the flow in a funnel as the opening angle and the initial film thickness, h_i are varied (the latter is controlled via varying fluid volume, V). The columns are the funnel angle, α , the initial fluid volume, V , the initial distance to the funnel centre, r_{c0} , the distance at which instability is observed, r_{c1} , the initial film height (in the z direction), h_i , and the number of fingers observed, N_{exp} . Errors reported are standard deviations. If no standard deviation is reported, only one video is available with a camera angle such that r_{c1} could be extracted. Full data sets for experiments carried out also using PDMS of different viscosity, for additional fluid volumes and recorded using different camera angles are available, see *Supplementary Table 1*.

undulations are present along the entire perimeter of the fluid front. We then need to extract the finger tip position for each finger. To that end, we define lines along the direction of motion of the fingers towards the funnel orifice. Figure 3(b) shows a few of these lines as an example. The lines are shown in red; they all converge in the funnel orifice. Along these lines, we extract pixel values from the frames in the videos, which for every frame yield an intensity profile as a function of r . Due to the dark front of the finger, every intensity profile has a clear step which can be fitted with an error function to obtain a finger tip position as a function of time. The intensity profiles extracted for every finger and every frame can be put together to form a kymograph, indicating qualitatively the finger tip dynamics for the tip considered. An example of such a kymograph is shown in figure 3(c). Note the linear part in the first few seconds of the kymograph, and the nonlinear slowing down for later times. Figure 3(d) zooms into the early times and confirms that the finger tip velocities are constant, and also that they depend on the opening angle, α . This figure shows few examples of finger tip position as a function of time for three different values of α . Tip positions are as measured from the finger starting point, which is always close to, but not exactly r_{c1} . Counterintuitively, the initial finger tip speed is larger for smaller α 's, another point to which we return in Sec. 4.2.

3. The model

In this section we discuss the appropriate model for a liquid film in a funnel. Consider a funnel of opening angle α , parametrized by

$$(x, y, z) = (r \cos \alpha \cos \theta, r \cos \alpha \sin \theta, r \sin \alpha), \quad r \in [R_l, R_r], \quad \theta \in [0, 2\pi],$$

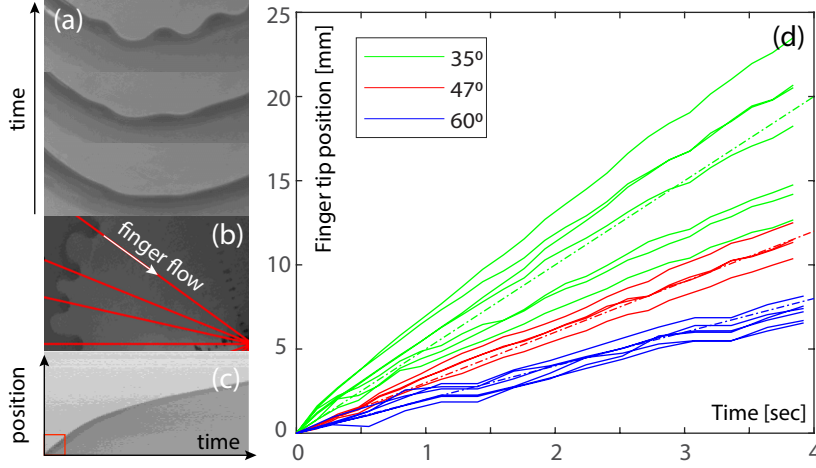


FIGURE 3. (a) Front propagation as a function of time for the setting from figure 2. The middle part shows the onset of fingers, where they become countable and at which point we define r_{c1} . (b) The dark front edge allows for finger tip position tracking along lines (red) of pixels towards the centre of funnel (orifice). (c) A kymograph for the 60 degree, $h_i = 5$ mm shows the tip position as a function of time. The initial part in the red square (duration of which is approximately 4 seconds) features an initially constant tip displacement rate. Examples of this initial finger tip position dynamics are shown in (d) for three different opening angles 60° , 47° , 35° and for the same initial $h_i = 5$ mm. Dash-dotted line are straight lines as a guide to the eye to show the average tip speed for each value of α . The time window shown in (d) corresponds approximately to the horizontal dimension of the red square in the kymograph shown in the part (c). Note an *increase* of the average speed with a *decrease* of α , the point discussed further in Sec. 4.2.

where $0 < R_l < R_r$. We can then define the orthogonal unit vectors on the funnel as

$$\mathbf{e}_1 = (\cos \alpha \cos \theta, \cos \alpha \sin \theta, \sin \alpha), \mathbf{e}_2 = (-\sin \theta, \cos \theta, 0), \mathbf{n} = (-\sin \alpha \cos \theta, -\sin \alpha \sin \theta, \cos \alpha),$$

where \mathbf{n} is the unit normal vector pointing inside the funnel, see figure 1(d). The principle normal curvatures in the directions parameterized by r and θ are given by $\kappa_1 = 0, \kappa_2 = \tan \alpha / r$. Based on Roy *et al.* (1997), the evolution of the thickness of a thin liquid film, h , inside a funnel can be described by the following partial differential equation

$$\left(1 - \frac{\tan \alpha}{r} h\right) h_t = -\frac{\gamma}{3\mu} \nabla_s \cdot \left[\left(h^3 - \frac{\tan \alpha}{2r} h^4 \right) \nabla_s \left(\nabla_s^2 h + \frac{\tan \alpha}{r - \tan \alpha h} \right) + \frac{\tan^2 \alpha h^4}{2r^3} \mathbf{e}_1 \right] - \frac{\rho g}{3\mu} \nabla_s \cdot \left[-\sin \alpha h^3 \left(1 - \frac{\tan \alpha}{r} h \right) \mathbf{e}_1 - \cos \alpha h^3 \nabla_s h \right], \quad (3.1)$$

where surface gradient, divergence and Laplace operators are defined by

$$\begin{aligned} \nabla_s f &= \frac{\partial f}{\partial r} \mathbf{e}_1 + \frac{1}{r \cos \alpha} \frac{\partial f}{\partial \theta} \mathbf{e}_2, \\ \nabla_s \cdot (q_1 \mathbf{e}_1 + q_2 \mathbf{e}_2) &= \frac{1}{r} \frac{\partial}{\partial r} (r q_1) + \frac{1}{r \cos \alpha} \frac{\partial}{\partial \theta} (q_2), \\ \nabla_s^2 f &= \frac{1}{r} \frac{\partial}{\partial r} (r f_r) + \frac{1}{r^2 \cos^2 \alpha} \frac{\partial^2 f}{\partial \theta^2}, \end{aligned}$$

respectively. We nondimensionalize the problem by $h = a \bar{h}, r = a \bar{r}, t = t_c \bar{t}$, where $a = \sqrt{\gamma / \rho g}$ is the capillary length, and $t_c = 3\mu a / \gamma$ is the timescale. Howell (2003)

pointed out that for a thin film such that $h \ll r/\tan(\alpha)$, the model can be simplified by neglecting asymptotically small terms; after dropping the bars, the governing equation is given by

$$\frac{\partial h}{\partial t} = -\nabla_s \cdot \left\{ h^3 \left[\nabla_s \left(\underbrace{\nabla_s^2 h}_{\text{surface tension}} + \underbrace{\frac{\tan \alpha}{r}}_{\text{substrate curvature}} \right) - \underbrace{\sin \alpha \mathbf{e}_1}_{\text{tangential gravity}} - \underbrace{\cos \alpha \nabla_s h}_{\text{normal gravity}} \right] \right\}. \quad (3.2)$$

For the experimental parameters given in Sec. 2, we have $a \approx 0.15$ cm and $t_c \approx 0.2$ s. For the consistency with the experiment, we choose the computational domain $r \in [1, L]$, $L = 100$, $\theta \in [0, 2\pi]$ and $h = O(1)$. The $r = 1$ is chosen as the domain boundary so to avoid the coordinate singularity at $r = 0$.

The computational results that we discuss in Sec. 4 are obtained by implementing second-order Crank-Nicolson method in time, second-order discretization in space and Newton's method to solve the nonlinear system at each time step, as described in detail in, e.g., [Lin & Kondic \(2010\)](#). To deal with the well-known issue of contact-line singularity, it is appropriate to introduce matched asymptotic expansions to join solutions in different length scales near the contact line, see [Snoeijer & Andreotti \(2013\)](#); [Sibley *et al.* \(2015\)](#) for further details. One can also introduce the interface potential that in general gives rise to an equilibrium film thickness. This film plays the role of a microscopic length scale that, again, has to be matched with outer solution where viscous forces are not important, see [Pismen & Eggers \(2008\)](#). We, however, for simplicity assume directly that the solid substrate is prewetted, i.e., already covered by a thin layer of fluid. Assuming the presence of such a prewetted layer essentially removes the contact line from the consideration. While various other models including relaxation of no-slip boundary condition exist and could be implemented, it is known that from the macro-scale point of view (that is, consideration of the film dynamics) what really matters is the lengthscale that is introduced by a model ([Diez *et al.* 2001](#)). In particular, for a simple and well researched constant flux flow down an incline (where time-independent influx leading to a fixed film thickness far behind the front is assumed), it is known that there is a translationally invariant solution for a film moving down an incline with the speed U that only weakly depends on the precursor film thickness, b_0 , as long as $b_0 \ll 1$ ([Bertozzi & Brenner 1997](#)). It should be noted though that the limit $b_0 \rightarrow 0$ is singular, leading to a shock-like singularity; the details of the film behavior in the presence of a vanishingly small length scale have been considered extensively in the literature, see, e.g. [Craster & Matar \(2009\)](#); [Bonn *et al.* \(2009\)](#); we do not discuss them further in the present work.

We note that while for a flow down an incline it can be assumed that the precursor film thickness is a constant (independent of position), for the flow in a funnel, conservation of fluid volume requires that the flux at inlet and outlet are the same. One simple choice of the boundary conditions that satisfies this condition is

$$h(r=1) = b_0 \left(\frac{\frac{1}{L} + L \cos \alpha}{1 + \cos \alpha} \right)^{1/3}, \quad h(L) = b_0, \quad \nabla_r (\nabla_r^2 h) - \cos \alpha \nabla_r h \Big|_{r=1, L} = 0. \quad (3.3)$$

The precursor film thickness $b(r)$ is obtained as the time-independent solution of one dimensional version of Eq. (3.2) (where the solution is assumed to be θ -independent), and with the boundary conditions as specified by Eq. (3.3). The solution of this nonlinear boundary value problem is found using Matlab's "fsolve".

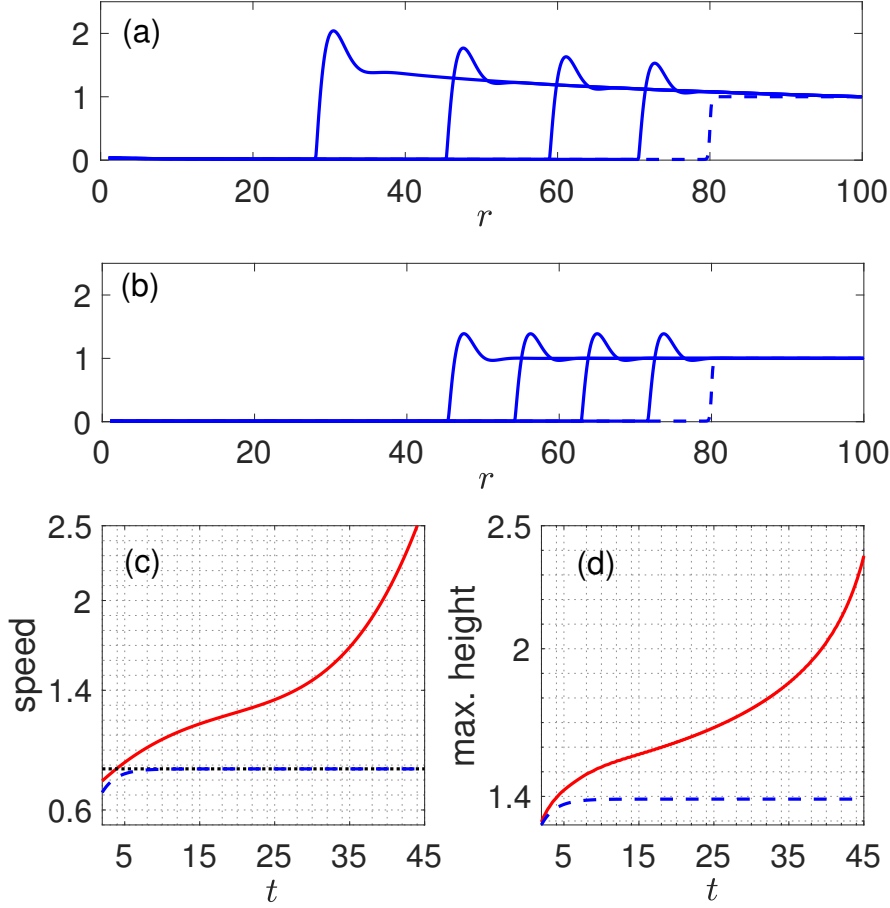


FIGURE 4. (Color online) Constant flux flow. (a) Funnel: azimuthally symmetric flow; (b) Incline: unperturbed flow (for simplicity we use the same variable r for the both flows; in (b) r stands for the downhill coordinate). The initial condition (dashed) for both (a) and (b) is specified by Eq. (4.1). The film profiles are shown at times 10, 20, 30 and 40 (solid lines). Panels (c-d) shows the speed (c) and the maximum height of the film (d) for the funnel flow (solid red) and for incline plane flow (dashed blue). The dotted (black) line in (c) shows the flow speed for a flow down an incline as discussed in the text; the difference between the computed and theoretical speed illustrates the (minor) influence of the initial transient behavior. Here, the inclination angle is $\alpha = 60^\circ$, the initial front position is $r_{c0} = 80$ and $b_0 = 0.01$.

4. Results

In this section we present the results of analysis, simulations and comparison between theoretical predictions with experiments. In Sec. 4.1 we focus on understanding the influence of funnel geometry on the flow without immediately attempting to develop direct comparison with the experiments. In this section we also discuss the insight that could be reached based on application of a self-similar type of approach. Then, in Sec. 4.2 we focus on the comparison of the theoretical and the experimental results. As we will see, an useful insight can be reached by developing a connection between the funnel flow and flow down an incline plane.

4.1. Film flow in a funnel: General considerations

4.1.1. Constant flux flow

For the incline plane flow, the best known case is the constant flux configuration and so we start by considering such a setup in a funnel. The initial film profile specified at $t = 0$ is a (smoothed) rectangular profile of the unit height as follows

$$h(r, t = 0) = b(r) + \frac{1 - b_0}{2} (1 + \tanh(5(r - r_{c0}))), \quad (4.1)$$

where r_{c0} corresponds to the front position. Figure 4(a) shows the profiles that develop at different times. To better illustrate the influence of funnel geometry on the flow, we also show in (b) the results for constant flux flow down an incline. The latter results are obtained by solving numerically Eq. (A 1) (see Appendix A), similar to the ones presented in e.g. Lin & Kondic (2010), with a uniform precursor film, $b(r) \equiv b_0$, and consistent boundary conditions. Both sets of simulations show the formation of a capillary ridge behind the front, as expected. The comparison of the results for the flow in a funnel and down an incline shows that for the former the film thickness is generally larger due to converging flow nature. Since the speed of the front is expected to scale with the film height as $U \propto h^2$ (Huppert 1982), this thickening also leads to a faster flow down a funnel compared to the flow down an incline, see figure 4(c). After initial transients, the latter evolves to a travelling wave moving with a constant speed, see figure 4 (c-d). Within the presently used scaling, this speed is given by $U \sim h^2 \sin \alpha$, see Appendix A and note that rescaled quantities are used there. The choice of relevant film thickness, h , entering this relation becomes more complicated for the constant volume flow, discussed in what follows.

Before proceeding with consideration of constant volume flow, we digress briefly to comment on the influence of precursor film thickness on the results. Figure 5 shows an example of the results obtained for $b_0 = 0.005, 0.01$ and 0.02 . We recall that for a film flowing down an incline plane in constant flux configuration, for larger precursor film thickness the spreading speed is (slightly) larger, see Appendix A. The same trend is found for the flow in a funnel, see figure 5(a, c). Figure 5(b) illustrates the steepening effect for the precursor film itself close to the funnel center, at small values of r .

4.1.2. Constant volume flow: Self-similar approach

Next we study the spreading of constant volume film in a funnel, focusing first on the insight that can be reached by considering the regimes where a self-similar solution can be formulated. For the flow down an incline, the self-similar solution (Huppert 1982) (ignoring surface tension effects), predicts that the front speed scales as $t^{-2/3}$, and the height behind the ridge, h_0 , as $t^{-1/3}$. The question is whether a similar approach could be used for the funnel flow.

Let us consider only the effect of substrate curvature and tangential gravity, and neglect all the other terms in Eq. (3.2). This simplification (valid sufficiently far behind the film front and for the opening angles which are not too small) leads to

$$h_t = \frac{1}{r} \left[r h^3 \left(\frac{\tan \alpha}{r^2} + \sin \alpha \right) \right]_r. \quad (4.2)$$

We observe that the substrate curvature amplifies the parallel component of gravity, and the amplification is larger when the flow is closer to the funnel centre. Next, we assume a solution of the form

$$h(r, t) = T(t)H(\eta), \quad \eta = \frac{R - r}{r_f(t)},$$

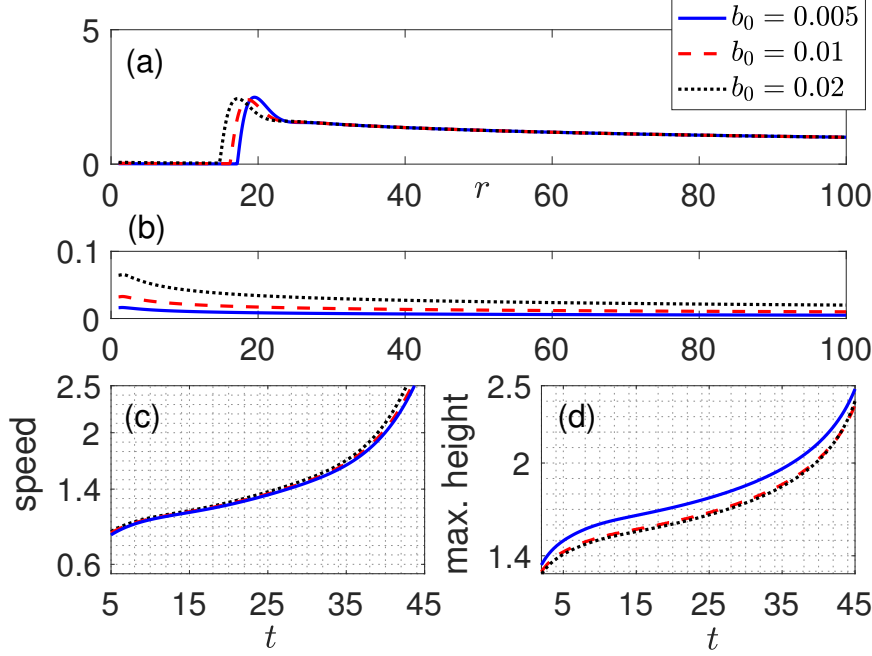


FIGURE 5. (Color online) Constant flux flow in a funnel: influence of the precursor film thickness for azimuthally symmetric flow. In all parts of the figure, the solid (blue), dashed (red) and dotted (black) lines corresponds to $b_0 = 0.005$, 0.01 and 0.02 , respectively. (a) Film profiles at $t = 45$, (b) precursor films, (c) speed of the spreading front, and (d) maximum film height. Here $\alpha = 60^\circ$ and $r_{c0} = 80$.

where R specifies the position of the uphill part of the deposited fluid (assumed to be a constant, which is a good approximation of the experiment, as discussed in Sec. 2), $r_f(t)$ is the distance travelled by the front and $R - r_f(t)$ is the position of the front, both at time t (we drop the specific dependence on t from now on). Equation (4.2) then leads to

$$\frac{\dot{T}r_f}{T\dot{r}_f}H - \eta H' = \frac{T^2}{\dot{r}_f} \left[\frac{r_f}{R - r_f\eta} \left(\sin \alpha - \frac{\tan \alpha}{(R - r_f\eta)^2} \right) H^3 - 3 \left(\sin \alpha + \frac{\tan \alpha}{(R - r_f\eta)^2} \right) H^2 H' \right], \quad (4.3)$$

where the over-dot notation denotes the time derivative, and primes denote the derivative with respect to η . The solution should satisfy the volume conservation condition

$$2\pi \int_{R-r_f(t)}^R rh(r, t) dr = 2\pi T r_f \int_0^1 (R - r_f\eta) H(\eta) d\eta = v_c, \quad (4.4)$$

where v_c is the fluid volume.

At early times after fluid deposition, $r_f \ll R$, and at the leading order in the small quantity r_f/R we obtain

$$\frac{\dot{T}r_f}{T\dot{r}_f}H - \eta H' = -3c_s \frac{T^2}{\dot{r}_f} H^2 H', \quad (4.5)$$

where $c_s = \sin \alpha + \tan \alpha / R^2$, and the volume constraint at the leading order reads

$$T r_f \int_0^1 H(\eta) d\eta = \tilde{v}_c, \quad (4.6)$$

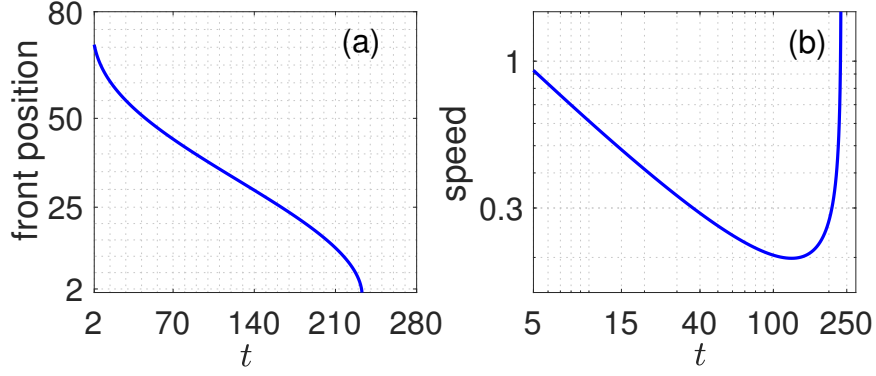


FIGURE 6. (Color online) Constant volume flow in a funnel: predictions based on self-similar approach. (a) Front position ($R - r_f$), (b) front speed (dr_f/dt) in Eqs. (4.10) and (4.11) (note log-log scale in (b)). Here $R = 90$ and $\hat{c} = 1370$, corresponding to the same funnel angle and volume used later in Fig. 7.

where $\tilde{v}_c = v_c/(2\pi R)$. We note that Eqs. (4.5) and (4.6) are identical to those derived for the incline plane problem (Huppert 1982). Simple scaling arguments give $T(t) \sim t^{-1/3}$, $r_f(t) \sim t^{1/3}$ and therefore the self-similar solution is

$$h(r, t) = \frac{1}{\sqrt{3c_s}} \sqrt{\frac{R-r}{t}}. \quad (4.7)$$

The volume conservation constraint, Eq. (4.6), gives the location of the leading edge

$$r_f(t) = \left(\frac{27c_s \tilde{v}_c^2}{4} \right)^{1/3} t^{1/3}, \quad (4.8)$$

and the film height at the front

$$h(r = R - r_f, t) = \left(\frac{\tilde{v}_c}{2c_s} \right)^{1/3} t^{-1/3}. \quad (4.9)$$

This result shows that, in the limit when the fluid front only travels a short enough distance, the flow down a funnel is identical to the flow down an incline plane, the result which may not be immediately obvious.

4.1.3. Constant volume flow: convergence effects

To gain some insight regarding the influence of the convergent nature of the funnel flow, we use the self-similar solution specified by Eq. (4.7) as an ansatz (but one should keep in mind that this solution is only valid for $r_f \ll R$) and require that the complete volume conservation constraint, Eq. (4.4), should be satisfied. Following this approach, we find that r_f satisfies the following equation

$$\frac{2R}{3} r_f^{3/2} - \frac{2}{5} r_f^{5/2} = \hat{c} \sqrt{t}, \quad (4.10)$$

where $\hat{c} = \sqrt{3c_s} v_c / 2\pi$. By taking the time derivative, we obtain the equation for the front speed

$$\frac{dr_f}{dt} = \frac{\hat{c}}{2(Rr_f^{1/2} - r_f^{3/2})\sqrt{t}}. \quad (4.11)$$

Figure 6 shows the solution for the front position ($R - r_f$) and the front speed (dr_f/dt). We see that the convergence effect leads to acceleration of the front for later times. To analyze this acceleration in more detail, we note that for the later stage of spreading, when the front is close to the funnel centre, we may assume $R - r_f \ll R$. For the discussion of this regime, it is convenient to introduce the stopping time $T_s = (4/(15\hat{c}))^2 R^5$, at which the fluid front reaches the funnel centre, $r_f(T_s) = R$. We can then rewrite Eq. (4.10) as

$$\frac{2}{3} \left(1 - \frac{R - r_f}{R}\right)^{3/2} - \frac{2}{5} \left(1 - \frac{R - r_f}{R}\right)^{5/2} = \frac{4}{15} \sqrt{1 - \frac{T_s - t}{T_s}}. \quad (4.12)$$

At the leading order in the small quantity $(R - r_f)/R$, we obtain $R - r_f = \sqrt{\frac{4R^2}{15T_s}} \sqrt{T_s - t}$. Therefore, the front speed \dot{r}_f scales as $(T_s - t)^{-1/2}$ showing that the front is expected to accelerate when approaching the funnel centre.

4.1.4. Constant volume flow: Numerical solution

Next, we study the spreading of a constant volume film in a funnel utilizing numerical simulations. The initial film profile at $t = 0$ is specified by the following expression

$$h(r, t = 0) = b(r) + \frac{1 - b_0}{2} (\tanh(5(r - r_{c0})) + \tanh(5(r_{c0} + w - r))), \quad (4.13)$$

where r_{c0} corresponds to the front position, and w determines the fluid volume. Figure 7 shows the film profiles, both for (a) funnel geometry and (b) for the same fluid volume travelling down an incline plane. For the flow down an incline, we observe film thinning, as expected. For the funnel flow, we observe different behaviour, with the thinning effect significantly reduced, or even inverted for the later times. As a consequence, the film in a funnel spreads significantly faster.

The parts (c) and (d) of this figure show that the scaling laws predicted by the self-similar solution (Huppert 1982) are accurately reproduced for the constant volume flow down an incline. Regarding the front speed shown in figure 7(c) and ignoring transient effects for very early times, the self-similar solution specified by Eq. (4.8) captures precisely its behaviour for early times, including the prefactor. Regarding figure 7(d), note that here we plot numerical result for the maximum film height, not the height behind the ridge to which the similarity solution applies; however, since the behaviour of the two considered quantities is essentially the same, the power law expected from the self-similar solution, Eq. (4.9), captures well the behavior of the maximum height for early times of the evolution, modulo a (constant) offset.

Focusing next on the funnel flow, we note the speed-up of the fluid front for the late times, as predicted by the self-similar solution derived in Sec. 4.1.2. This speed-up is not as strong as predicted (viz. figure 6(b)), which is not surprising since the self-similar approach is not expected to be accurate for late times. Figure 7(d) also shows the corresponding increase of the film height. This thickening effect, which is also relevant for the intermediate times shown in figure 7, is responsible for the deviation from the spreading law predicted by the self-similar solution (note deviation of the slope of the red lines in figure 7, parts (c) and (d), from the scaling expected by the self-similar solution for the flow down an incline).

Figure 8 shows the results obtained for the constant volume flow in the funnel geometry as the opening angle, α , is varied. The film spreads faster down a funnel characterized by larger α , as shown in part (a). We suspect that the tangential gravity may have dominant effect on the time scale of the flow; to show that this is the case, we plot the results for the front position and maximum film height versus $t \sin \alpha$ in the parts (b) and (c). We find

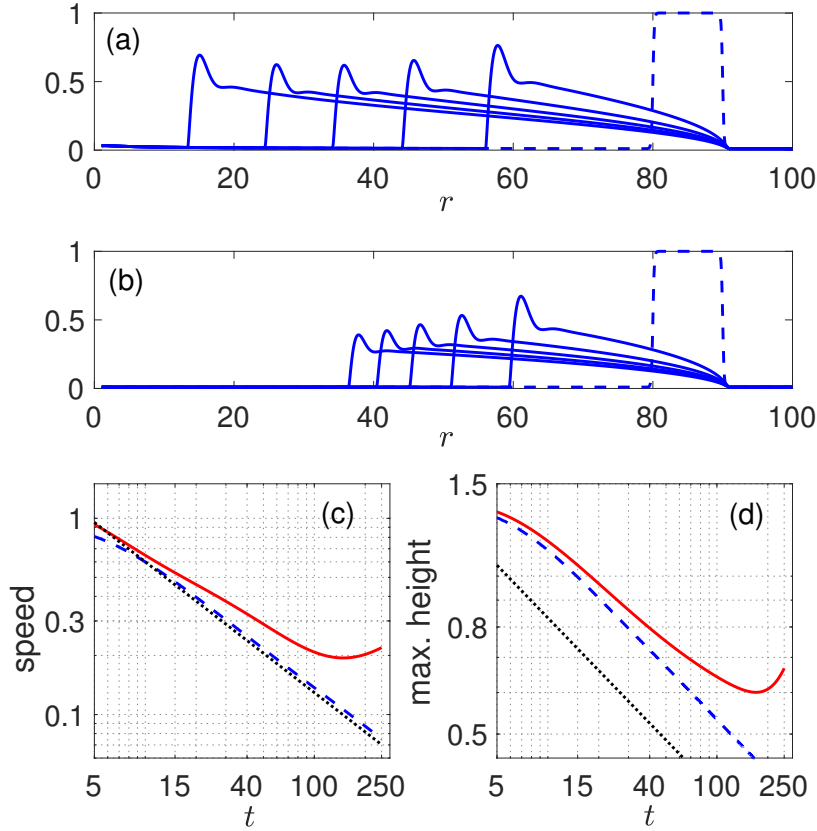


FIGURE 7. (Color online) Constant volume flow. (a) Funnel: azimuthally symmetric flow; (b) Incline: unperturbed flow. The initial condition (dashed) is the same for (a - b) and is specified by Eq. (4.13). The film profiles are shown at times 50, 100, 150, 200, and 250 (solid lines). (c - d) The speed (c) and the maximum height of the film (d) for the funnel flow (solid red) and incline plane flow (dashed blue) (note log-log scale). The dotted (black) lines in (c) and (d) plot the self-similar solutions (Eq. (4.8 - 4.9)), respectively; note that Eq. (4.9) applies to the thickness behind the capillary ridge, leading to an approximately constant offset to the numerical solution for the maximum height. Slight deviation of the numerical solution from the expected scaling for very early times illustrate the minor influence of the initial transient behavior. Here, the inclination angle is $\alpha = 60^\circ$, the initial front position is $r_{c0} = 80$, $w = 10$ and $b_0 = 0.01$.

approximate collapse of the front position curves in the part (b), showing that indeed the tangential gravity plays the major role. Regarding the maximum film height shown in the part (c), we observe that this quantity is larger for larger α 's, as expected since the capillary ridge is more pronounced for such angles (we expect that this effect is also responsible for slightly faster spreading for larger α 's observed in part (b)). However, the trend of the maximum heights is similar for all α 's, with the film height decreasing for early times, while at the later times when the front reaches closer to the funnel centre, the film height increases, see part (c), and faster spreading is observed, see part (b).

4.1.5. Instability development

To obtain a basic idea regarding instability development (finger formation), we discuss first the flow down an incline plane for the constant flux configuration. In such a setup, the base state (for which the film thickness does not depend on the transverse coordinate),

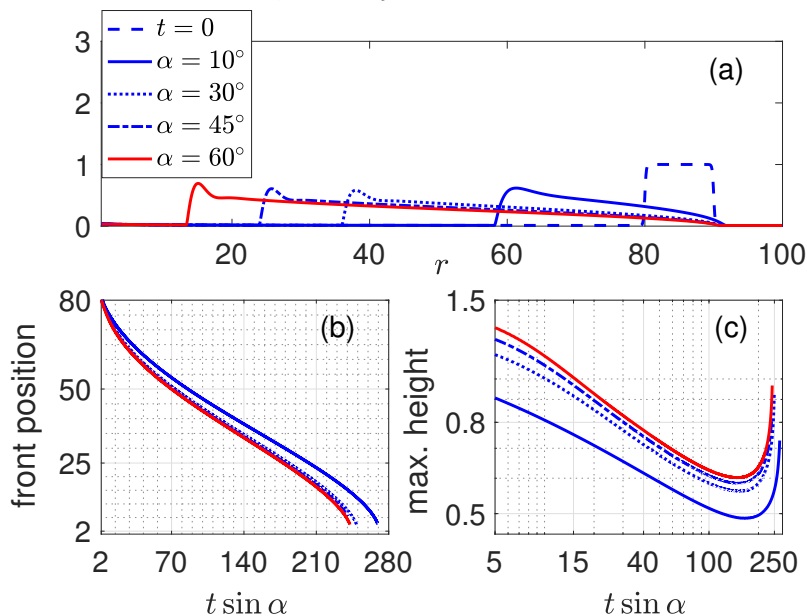


FIGURE 8. (Color online) Funnel flow: Constant fluid volume spreading as the opening angle α is varied. (a) Film profiles at $t = 250$. The initial conditions are taken to be the same, shown by the dashed line. The position of the spreading front and the maximum film height are shown in (b) and (c), respectively (note log-log scale in (c)). Here, the initial front position is $r_{c0} = 80$, $w = 10$ and $b_0 = 0.01$.

translates down an incline at a constant speed U , as already discussed. This fact allows for carrying out the linear stability analysis in the moving frame translating (with speed U) with the film itself; in this frame the base state is time independent (Bertozzi & Brenner 1997). Appendix A briefly outlines this problem, and discusses in particular the wavenumber of maximum growth, q_m , the corresponding wavelength, $\lambda_m = 2\pi/q_m$, as well as the critical wavenumber q_c , such that the wavenumbers $q > q_c$ are stable; see figure 12 in the Appendix A. The stability analysis becomes more complicated for the constant volume flow down an incline, see Gomba *et al.* (2007), since for that problem the base state itself is evolving, as also illustrated in figure 7(b). For the flow in a funnel, viz. figure 7(a), an additional complication involves gradual thickening of the film due to convergent flow.

In Sec. 4.2 we will consider rather simple approach to utilize the LSA results in the incline plane problem to compare with experiment; here we outline the basic aspect of this approach, without explicit reference to the experiment. Let us consider constant volume flow in a funnel, as shown in figure 9. When the film front has reached a prescribed position for the considered opening angle, α , the thickness h_0 is extracted from the film profile as the thickness at the inflection point behind the capillary ridge. With the knowledge of this characteristic thickness, h_0 , and the opening angle, α , we can then find a travelling wave solution on an incline plane that has exact the same characteristic thickness; such solution is plotted in figure 9 as well (marked by P). The LSA results of this travelling wave solution then gives us the most unstable wavenumber. Therefore, this most unstable wavenumber results from combination of the information from experiments (instability location), numerical simulations of funnel flow (providing h_0), and the LSA originating from the flow down an incline plane. In the next section, we discuss how to

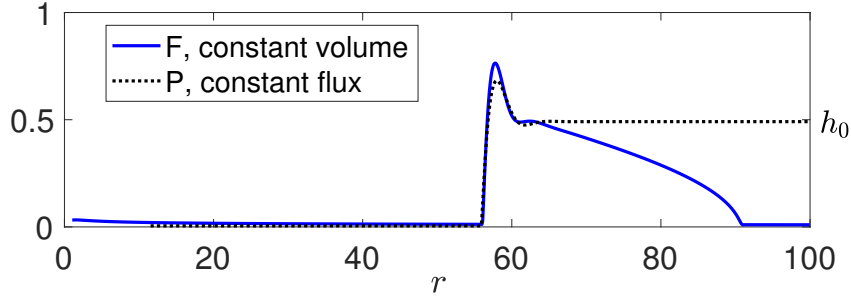


FIGURE 9. (Color online) Film profiles in a funnel ('F', constant volume) and on an incline plane ('P', constant flux). The former one is the film profile at $t = 50$ in figure 7(a). The later one is a travelling wave solution with the film thickness behind the front corresponding to the thickness at the inclination of point of 'F'. This thickness, h_0 , determines the scale that is used in the LSA.

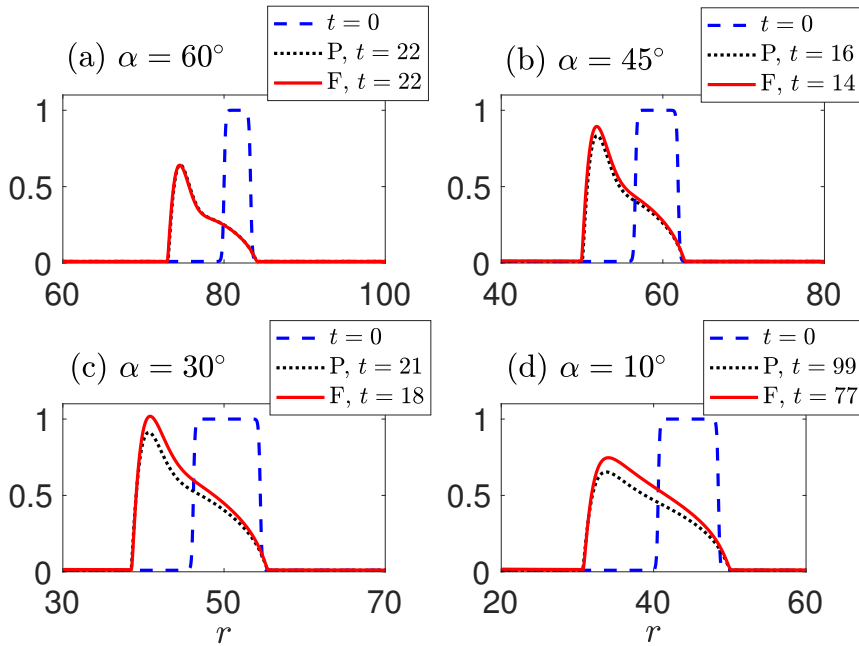


FIGURE 10. (Color online) Time evolution of a film on an incline plane ('P') and in a funnel ('F'). The initial condition is specified by Eq. (4.13). The results are plotted at the times at which experimentally observed instability radius, r_{c1} , is reached. Note that the shown range of r , 40, is the same for all figure parts. The initial volume correspond to the experimentally used one for the film height of 5 mm for $\alpha = 60^\circ$, 47° , 35° , and of 2.5 mm for $\alpha = 11^\circ$, see Table 1.

use similar approach to provide basic understanding of the instability development in experiment.

4.2. Film flow in a funnel: Comparison with the experiment

We now proceed to the consideration of a funnel flow, but with the specific emphasis on the comparison with the experiments. While we will modify the choice of the parameters that we use to more closely resemble the experimentally relevant ones, for simplicity

we still keep the smoothed rectangular initial profile, with the idea that the instability takes some time to develop, and therefore the initial film profile is not of relevance. However, we do choose the initial film width, w , see Eq. (4.13), so to be consistent with the experimental fluid volume (in units of a^3) by $V = 2\pi Sh_0 w$, with S in units of a and $h_0 = 1$. We note that the choice that has been made in selecting the parameters (in particular, having fixed film thickness and varying fluid volume as the opening angle α is modified) simplifies the connection to the experiments; the price to pay is the increased complexity of the results, in particular when discussing the trends of the results as α is modified, as we will see in what follows.

Figure 10 shows the results for both funnel simulations (marked by ‘F’) and for the same fluid volume travelling down an incline plane (marked by ‘P’), for the fluid volumes corresponding to the experimental ones. When comparing the thicknesses of the capillary ridge between funnel and incline plane flow, the effects related to convergent nature of the funnel flow become relevant, as discussed in Sec. 4.1.4. In particular, when considering the change of the capillary ridge thickness as the opening angle α is varied, we need to remember that in the simulations the volume increases as α decreases from 60° to 45° and 30° (to keep approximate consistency with the experiments), leading to thicker films and ridges. † The influence of the volume increase is visible in figure 10, where we observe non-monotonous dependence of the capillary ridge thickness on α .

Next we proceed with application of the LSA to the present problem. To make progress, we choose an approach that allows us to reach a basic understanding of the instability development observed in the experiments. The LSA, as already discussed, is based on the incline plane problem and the constant flux setup, using the film thickness behind the capillary ridge, h_0 , as the appropriate scale, see figure 9. We assume that the film is initially deposited at $r = r_{c0}$, so that the fluid volume forms a circle of radius $r_{c0} \cos \alpha$. As the film flows down a funnel, the radius of this circle, $r_c(t)$, becomes smaller, and the film itself thins (for the chosen initial condition). To make a comparison with experiments, we choose the characteristic thicknesses, h_0 , as the thickness obtained from simulations at the time when the film front reaches r_{c1} , where the onset of fingering extracted from the experimental results occurs, as illustrated in figure 10. Table 2 lists the values of $h_0(r_{c1})$ for a few values of α and for the widths w of the initial condition that lead to the experimental fluid volumes. Additional simulations (not shown for brevity) show that $h_0(r_{c1})$ is essentially the same for any reasonable choice of the initial fluid geometry.

Figure 11 plots the obtained results for the most unstable wavelength predicted by the LSA together with the experimentally measured one; the LSA results are also shown in Table 2. The experimental wavelength is defined by $\lambda = 2\pi \cos(\alpha)r_c/N_{\text{exp}}$, and is given in units of the capillary length. We note that it is crucial to use the film thickness $h_0(r_{c1})$ when comparing the predictions of the LSA and experiment: using the initial film thickness does not lead to a meaningful agreement. The number of fingers predicted by the LSA, N_{LSA} (given also in Table 2), can be compared directly with the values obtained in the experiments, N_{exp} , see Table 1. We find that the agreement is excellent for larger opening angles, however for small angles the most unstable wavelength found by the LSA is larger than the experimental one. There is a number of possible reasons for this difference, including an increased influence of the azimuthal curvature that is not included in the presented methodology (note that r_{c1} is smaller for small α ’s), or simply the fact that slow development of instability for small values of α may involve additional

† Since we are interested more in the trends than in exactly matching theory with experiments, we keep round numbers for the angles that we use, since the differences in the results are minor.

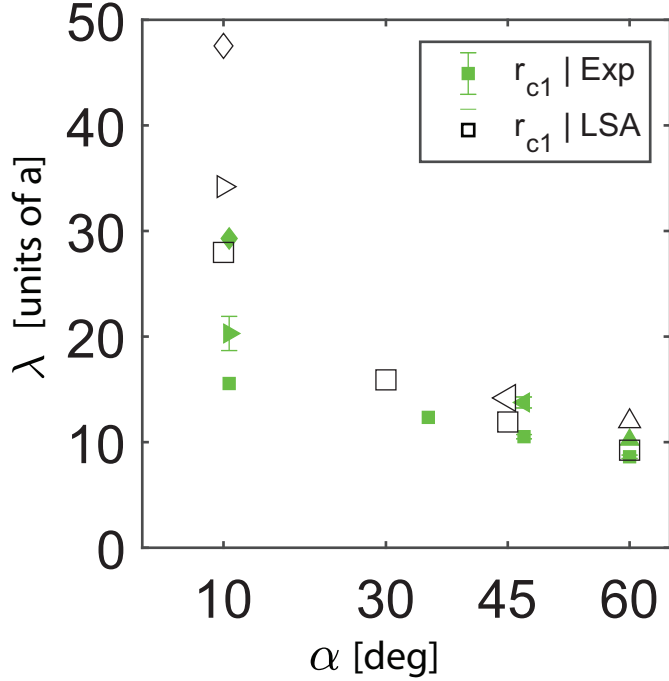


FIGURE 11. (Color online) Funnel: average finger spacing wavelength, λ , versus opening angle, α , including experiments (Exp, filled green symbols) for which r_{c1} is available (see Table 1), as well as matching linear stability analysis (LSA, open black symbols) predictions from Table 2. For completeness we plot the results for all available values of h_i per angle. Symbols indicate h_i . \square : $h_i = 5$ mm for 60° , 47° , 35° , and $h_i = 2.5$ mm for 11° ; \triangle : $h_i = 7$ mm for 60° ; \triangleleft : $h_i = 7$ mm for 47° ; \triangleright : $h_i = 3$ mm for 11° ; \diamond : $h_i = 4$ mm for 11°

effects, such as transient growth mechanism which was proposed for the flow down an incline (Bertozzi & Brenner 1997).

Next, we proceed with explanation (at least in qualitative terms) of some perhaps counterintuitive trends of the experimental results. Figure 3(d) shows an *increase* of the finger tip speed as the opening angle is *decreased*. Measuring the typical slopes in this figure, we find that finger tip speed increases by the factors of (approximately) 1.5 and 2.5 as the opening angle decreases from $\alpha = 60^\circ$ to 47° and 35° , respectively. Recalling now the expected scaling for the front speed, $U \sim h_0^2 \sin \alpha$, and using the values for h_0 at the instability onset from Table 2, we find that this expression for U provides a good approximation for the front tip speed (the corresponding ratios are approximately 1.8 and 2.2). Therefore, an increase of the value of h_0 as the opening angle decreases has stronger influence than a decrease of $\sin(\alpha)$. One should keep in mind of course that the above expression for U applies to an unperturbed front while the experimental results from figure 3 are obtained by measuring the tip speed, and therefore only approximate agreement could be expected.

To explain an increase of the typical instability wavelength as α is decreased, recall that based on the standard scaling argument, the (dimensional) most unstable wavelength scales with the film thickness behind the front, h_0 , see Appendix A. Note that this scaling argument is approximate only, since based on the LSA for the constant flux flow down an incline, see figure 12 in Appendix A, the inclination angle influences the most unstable

α (degrees)	w	r_{c1}	$h_0(r_{c1})$	q_m	q_c	λ_m	N_{LSA}
60	3.3	73.0	0.3	0.68	1.15	9.24	25
	6.4	74.7	0.6	0.52	0.89	11.97	20
45	5.3	50.0	0.45	0.53	0.89	11.91	19
	10.5	48.0	0.69	0.44	0.75	14.19	15
30	8.3	38.5	0.59	0.40	0.67	15.90	13
10	7.9	30.7	0.56	0.22	0.37	27.97	6
	11.4	33.3	0.73	0.18	0.29	34.20	6
	21.0	28.7	0.99	0.13	0.21	47.53	3

TABLE 2. Results and predictions of the linear stability analysis for the experimental fluid volumes. The initial film thickness $h_0(r_{c0}) = 1.0$. The columns are as follows: α : the funnel opening angle, similar to the experimental values, see Table 1; w : the width of the initial condition in time-dependent simulations as used in figure 10, r_{c1} : the position at which instability is observed in the experiments; h_0 at r_{c1} , as obtained in the simulations for funnel flow, see the text for details; q_m : the most unstable wavenumber obtained by the LSA; q_c : critical wavenumber obtained by the LSA; $\lambda_m = 2\pi/q_m$; N_{LSA} : prediction for the number of fingers based on λ_m and r_{c1} . The values used for r_{c0} (initial front position) and coming from the experiments and are listed in Table 1; note that the listed values of w combined with the specified values of r_{c0} and $h_0(r_{c0})$ lead to the same fluid volume as in the experiments.

wavelength as well. Still, the scaling $\lambda_m \propto h_0(r_{c1})$ appears to be a good description of the experimental results, as it can be seen from Tables 1 and 2.

4.2.1. Discussion

Reasonable agreement between theory and experiments, in particular for larger opening angles, shows that our approach combining the information from experiments, simulations, and LSA describes well the main features of instability development. Before closing this section, we list few additional comments and observations.

- The reader may wonder whether simply using h_i from the experiments (see Table 1) could be used to describe the instability development and emerging lengthscales. This approach however does not lead to a reasonable estimate, since there is a considerable change in the film thickness between r_{c0} and r_{c1} . One may also wonder whether the results of LSA may depend on the initial condition in simulations (which is chosen ad hoc): the answer is again no, since the film does not develop instability immediately; by the time r_{c1} is reached, the memory of the initial condition is lost.

- There are two main differences between the flow down an incline and in a funnel: one of them is film thickening due to convergent nature of the flow, as discussed in Sec. 4.1.2 and 4.1.4; the other one is the presence of azimuthal curvature for the funnel flow, that we have not discussed in much detail. The curvature in the azimuthal direction scales as $1/r$, see Section 3, so it is a small quantity as long as only large values of r are considered. This value should be compared with the typical curvature (in the radial direction) of the film itself, which is an $O(1)$ quantity close to the film front. Smallness of the azimuthal curvature justifies ignoring it in the present work, since it is expected to become important only very close to the funnel centre. Therefore, as long as the fluid front is far away from the centre, the flow in a funnel is similar to the flow down an

incline plane, as long as the fact that the film thickens due to volume conservation is taken into account.

- Figure 10 specifies the times at which instability starts to develop (when the fluid front reaches r_{c1}). We note that these times are shorter for the funnel compared to flow down an incline, in particular for smaller α 's; this is due to the film thickening for the flow in a funnel. Thicker films flow faster and also become unstable sooner, compared to the flow down an incline.

- In light of the discussion in this section, the experimental fact that the observed number of fingers does not depend on fluid viscosity (see *Supplementary Table 1*) may not be obvious. While viscosity only changes the time scale of the flow, for the present problem the time scale may be important since the film thickness changes with time. However, the location at which film becomes unstable, r_{c1} , and the film thickness behind the capillary ridge, h_0 , turn out not to depend on the fluid viscosity, supporting the presented approach for carrying out the LSA and interpretation of the results.

- The LSA predicts that instability will develop if the circumference $2\pi r_c \cos \alpha$ is larger than $\lambda_c = 2\pi/q_c$. Consistently, the maximum number of unstable modes (leading to fingers in experiments) that can be supported is $\lfloor 2\pi r_c \cos \alpha / \lambda_c \rfloor$, where $\lfloor \cdot \rfloor$ is the floor function. One untested consequence of this result is that if the film is released close to the centre of the funnel, it may not become unstable since the circumference of the circle formed by the initial fluid front may not be long enough to support instability development.

5. Conclusions

The presented results show that a reasonably complete understanding of instability development for a film flowing in a funnel can be reached by combining the insight from experiments and asymptotic analysis that allows for significant simplification of the governing equations. Furthermore, it turns out that despite the complexity of the problem, a useful insight can be also reached by considering a self-similar approach similar to the one used for the flow down an incline plane. Such insight from self-similar methods combined with linear stability analysis originated from the flow down an incline provides an important guidance in carrying out numerical simulations that help to develop better understanding of the instability development. While we have focused on a particular geometry of flow in a funnel, we note that a similar approach could be applied to a number of other unstable flows, such as the flows on a sphere, outside surface of a funnel, or even in more complicated geometries.

To conclude, we note that instabilities of the systems whose base state evolves in time are difficult to analyze in a tractable manner. For the present problem, we have shown that a reasonably good insight can be reached by simplifying the problem first, and then using some input regarding instability development from the experiments. One would of course like to be able to understand the general features of instability development, including the factors that govern instability onset itself. Reaching this goal will require further development of stability analysis and is left as an open problem for future work.

Acknowledgements We thank Vittorio Saggiomo for help with 3D printing of the funnels, to the undergraduate students Elliot Figueroa, Jody Parchment and Yimei Xu (supervised by Ryan Allaire) for help with the experiments and data analysis as a part of their Capstone class at NJIT. TSL acknowledges support by Ministry of Science and Technology, Taiwan, under research grant MOST-109-2115-M-009-006-MY2, and LK by the NSF grants CBET-1604351 and DMS-1815613.

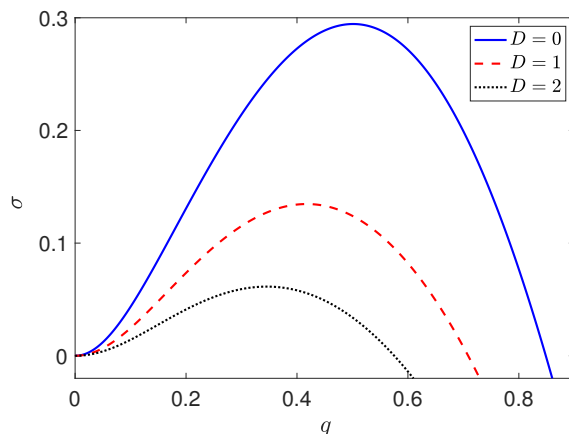


FIGURE 12. (Color online) Results of LSA for liquid film on an incline plane with different D . The precursor film thickness is $b_0 = 0.01$.

Appendix A. Stability of the constant flux flow down an incline plane

Consider a completely wetting fluid flowing down a planar surface enclosing an angle α with the horizontal. With the same scales as used in the main body of the paper, the evolution equation of the film thickness can be written as (see, e.g., (Bertozzi & Brenner 1997; Kondic 2003))

$$\frac{\partial}{\partial t} h = -\nabla \cdot [h^3 \nabla^3 h - \cos \alpha h^3 \nabla h + \sin \alpha h^3 \mathbf{e}_x], \quad (\text{A } 1)$$

where \mathbf{e}_x is the unit vector pointing in the positive x -direction. Re-normalizing the variables as $h = h_0 \bar{h}$, $t = \bar{t}/(h_0^5 \sin^4 \alpha)^{1/3}$, $x = (h_0/\sin \alpha)^{1/3} \bar{x}$, one obtains the well-known model of thin liquid film (after dropping the bars)

$$\frac{\partial}{\partial t} h = -\nabla \cdot [h^3 \nabla^3 h - D h^3 \nabla h + h^3 \mathbf{e}_x], \quad (\text{A } 2)$$

where $D = (h_0/\sin \alpha)^{2/3} \cos \alpha$. This equation admits a one-dimensional travelling wave solution satisfying

$$-U h + h^3 h_{xxx} - D h^3 h_x + h^3 = c, \quad (\text{A } 3)$$

where boundary conditions $h(x = \infty) = b_0$, $h(x = -\infty) = 1$ are imposed to have $U = 1 + b_0 + b_0^2$, $c = -(b_0 + b_0^2)$. (Note that the (unscaled) speed of the front scales with the film thickness squared, as it can be seen from the ratio of the scaling factors for x and t .) Linear stability of the film with respect to perturbations in the transverse, y , direction is conveniently carried out in a moving coordinate frame, $s = x - Ut$, where we assume the solution of the form

$$h(s, y, t) = H(s) + \epsilon g(s) e^{\sigma t} e^{iqy}, \quad (\text{A } 4)$$

where $H(s)$ satisfies (A 3). At $O(\epsilon)$ we obtain a linear eigenvalue problem for $g(s; q)$ with eigenvalue σ that represents the growth rate of temporal evolution of the perturbation at each wave number. Figure 12 shows the results of this analysis; for more details see e.g. Kondic (2003).

REFERENCES

- BACKHOLM, M., BENZAQUEN, M., SALEZ, T., RAPHAËL, E. & DALNOKI-VERESS, K. 2014 Capillary levelling of a cylindrical hole in a viscous film. *Soft Matter* **10**, 2550–2558.
- BALESTRA, G., BADAOU, M., DUCIMETIÈRE, Y.-M. & GALLAIRE, F. 2019 Fingering instability on curved substrates: optimal initial film and substrate perturbations. *J. Fluid Mech.* **868**, 726.
- BERTOZZI, A. L. & BRENNER, M. P. 1997 Linear stability and transient growth in driven contact lines. *Phys. Fluids* **9**, 530.
- BONN, D., EGGERS, J., INDEKEU, J., MEUNIER, J. & ROLLEY, E. 2009 Wetting and spreading. *Rev. Mod. Phys.* **81**, 739.
- BOSTWICK, J. B., DIJKSMAN, J. A. & SHEARER, M. 2017 Wetting dynamics of a collapsing fluid hole. *Phys. Rev. Fluids* **2**, 014006.
- BRANDÃO, R., FONTANA, J. V. & MIRANDA, J. A. 2014 Suppression of viscous fingering in nonflat hele-shaw cells. *Phys. Rev. E* **90**, 053003.
- CRASTER, R.V. & MATAR, O.K. 2009 Dynamics and stability of thin liquid films. *Rev. Mod. Phys.* **81**, 1131.
- DAVIS, S. H. 1980 Moving contact lines and rivulet instabilities. Part I: The static rivulet. *J. Fluid Mech.* **98**, 225.
- DE GENNES, PIERRE-GILLES, BROCHARD-WYART, FRANÇOISE & QUÉRÉ, DAVID 2004 *Capillarity and wetting phenomena: drops, bubbles, pearls, waves*. Springer Science & Business Media.
- DIEZ, J. A., GONZÁLEZ, A. & KONDIC, L. 2009 On the breakup of fluid rivulets. *Phys. Fluids* **21**, 082105.
- DIEZ, J. A., GRATTON, J. & GRATTON, J. 1992 Self-similar solutions of the second kind for a convergent viscous gravity current. *Phys. Fluids A* **4**, 1148.
- DIEZ, J. A., KONDIC, L. & BERTOZZI, A. L. 2001 Global models for moving contact lines. *Phys. Rev. E* **63**, 011208.
- DIJKSMAN, J. A., MUKHOPADHYAY, S., BEHRINGER, R. P. & WITELSKI, T. P. 2019 Thermal Marangoni-driven dynamics of spinning liquid films. *Phys. Rev. Fluids* **4**, 084103.
- DUKLER, Y., JI, H., FALCON, C. & BERTOZZI, A. L. 2020 Theory for undercompressive shocks in tears of wine. *Phys. Rev. Fluids* **5**, 034002.
- FRAYSSE, N. & HOMSY, G. M. 1994 An experimental study of rivulet instabilities in centrifugal spin coating of viscous Newtonian and non-Newtonian fluids. *Phys. Fluids* **6**, 1491.
- GOMBA, J. M., DIEZ, J., GRATTON, R., GONZALEZ, A. G. & KONDIC, L. 2007 Stability study of a constant-volume thin film flow. *Phys. Rev. E* **76**, 046308.
- GONZALEZ, A. G., DIEZ, J. D. & KONDIC, L. 2013 Stability of a liquid ring on a substrate. *J. Fluid Mech.* **718**, 213.
- GOODWIN, R. & HOMSY, G. M. 1991 Viscous Flow down a slope in the vicinity of a contact line. *Phys. Fluids A* **3**, 515.
- HO, C. C. & KHEW, M. C. 2000 Surface free energy analysis of natural and modified natural rubber latex films by contact angle method. *Langmuir* **16**, 1407–1414.
- HOWELL, P. D. 2003 Surface tension driven flow on a moving curved surface. *J. Eng. Math.* **45**, 283–308.
- HUPPERT, H. 1982 Flow and Instability of a viscous current down a slope. *Nature* **300**, 427.
- KONDIC, L. 2003 Instabilities in gravity driven flow of thin fluid films. *SIAM Review* **45**, 95.
- KONDIC, L. 2019 Capstone Laboratory. <http://cfsm.njit.edu/capstone/projects/2019/main.php>.
- LIN, T.-S., DIJKSMAN, J. & KONDIC, L. 2020 See supplementary material.
- LIN, T.-S. & KONDIC, L. 2010 Thin films flowing down inverted substrates: Two dimensional flow. *Phys. Fluids* **22**, 052105.
- LV, C., EIGENBROD, M. & HARDT, S. 2018 Stability and collapse of holes in liquid layers. *J. Fluid Mech.* **855**, 1130–1155.
- MARCHAND, A., DAS, S., SNOEIJER, J. H. & ANDREOTTI, B. 2012 Contact angles on a soft solid: From Young's Law to Neumann's Law. *Phys. Rev. Lett.* **109**, 236101.
- MAYO, L. C., MCCUE, S. W. & MORONEY, T. J. 2013 Gravity-driven fingering simulations for a thin liquid film flowing down the outside of a vertical cylinder. *Phys. Rev. E* **87**, 053018.

- MELO, F., JOANNY, J. F. & FAUVE, S. 1989 Fingering Instability of Spinning Drops. *Phys. Rev. Lett.* **63**, 1958.
- MIRANDA, J. A., PARISIO, F., MORAES, F. & WIDOM, M. 2000 Gravity-driven instability in a spherical hele-shaw cell. *Phys. Rev. E* **63**, 016311.
- ORON, A., DAVIS, S. H. & BANKOFF, S. G. 1997 Long-scale evolution of thin liquid films. *Rev. Mod. Phys.* **69**, 931.
- PISMEN, L. M. & EGGERS, J. 2008 Solvability condition for the moving contact line. *Phys. Rev. E* **78**, 056304.
- ROY, R. V., ROBERTS, A. J. & SIMPSON, M. E. 1997 A lubrication model of coating flows over a curved substrate in space. *J. Fluid Mech.* **454**, 235–261.
- SIBLEY, D., NOLD, A. & KALLIADASIS, S. 2015 The asymptotics of the moving contact line: cracking an old nut. *J. Fluid Mech.* **764**, 445–462.
- SMOLKA, L. & SEGALL, M. 2011 Fingering instability down the outside of a vertical cylinder. *Phys. Fluids* **23**, 092103.
- SNOELJER, J. H. & ANDREOTTI, B. 2013 Moving contact lines: Scales, regimes, and dynamical transitions. *Annu. Rev. Fluid Mech.* **45**, 269–292.
- TAKAGI, D. & HUPPERT, H. E. 2010 Flow and instability of thin films on a cylinder and sphere. *J. Fluid. Mech.* **647**, 221–238.
- TROIAN, S. M., HERBOLZHEIMER, E., SAFRAN, S. A. & JOANNY, J. F. 1989 Fingering Instabilities of Driven Spreading Films. *Europhys. Lett.* **10**, 25.
- ZHANG, Y., VANDAELE, A., SEVENO, D. & CONINCK, J. DE 2018 Wetting dynamics of polydimethylsiloxane mixtures on a poly(ethylene terephthalate) fiber. *J. Coll. Interface Sci.* **525**, 243–250.
- ZHENG, Z., FONTELOS, M. A., SHIN, S., DALLASTON, M. C., TSELUIKO, D., KALLIADASIS, S. & STONE, H. A. 2018 Healing capillary films. *J. Fluid Mech.* **838**, 404–434.